Article

Spacetime magnetic hopfions from internal excitations and braiding of skyrmions

Check for updates

Ross Knapman [1,2], Timon Tausendpfund [2], Sebastián A. Díaz [1,3] & Karin Everschor-Sitte [1] ✉

Spatial topology endows topological solitons, such as skyrmions and hopfions, with fascinating dynamics. However, the temporal dimension has so far provided a passive stage on which topological solitons evolve. Here we construct spacetime magnetic hopfions: magnetic textures in two spatial dimensions that when excited by a time-periodic drive develop spacetime topology. We uncover two complementary construction routes using skyrmions by braiding their center of mass position and by controlling their internal low-energy excitations. Spacetime magnetic hopfions can be realized in nanopatterned grids to braid skyrmions and in frustrated magnets under an applied AC electric field. Their topological invariant, the spacetime Hopf index, can be tuned by the applied electric field as demonstrated by our collective coordinate modeling and micromagnetic simulations. The principles we have introduced to actively control spacetime topology are not limited to magnetic solitons, opening avenues to explore spacetime topology of general order parameters and fields.

Topological solitons are robust localized structures actively studied by disciplines ranging from cosmology[1,2] and particle physics[3–6] to optics[7–10] and condensed matter[11–13]. Despite the differences across the many systems where they form, topological solitons exhibit enhanced stability which is due to the nontrivial topology of their structure in space. In contrast, the temporal dimension does not play a role in defining soliton topology.

Topological solitons in magnets include skyrmions and hopfions[14–20]. The skyrmion topology is determined by the number of times the magnetization wraps the unit sphere. On the other hand, the hopfion structure rests on curves in space where the magnetization points in the same direction, its preimages[21–25]. How often any two preimages wind around each other is counted by the Hopf index[21], the invariant that characterizes hopfion topology. Although skyrmions and hopfions exhibit fascinating dynamics, it is rooted exclusively in their spatial topology, a property of their spatial structure that they carry as they evolve in time.

However, robust structures in time, including spacetime crystals in magnets, have been recently reported[26–30]. These reports motivate the question of the existence of topological solitons with time involved fundamentally and inextricably. Here we turn to magnetic textures in two spatial dimensions and their time evolution to construct topological magnetic solitons in spacetime. Since their nontrivial spacetime topology is characterized by an extension of the Hopf index, we name them spacetime magnetic hopfions.

Results

Spacetime magnetic hopfions require a time-periodic magnetization provided by an externally applied drive. The physical difference between generic magnetic solitons and spacetime magnetic hopfions lies in their nontrivial spacetime topology, which affords them robustness against time-dependent perturbations.

Spacetime topology construction

To construct spacetime magnetic hopfions we exploit the topology of regular hopfions.

A hopfion in three spatial dimensions results from the following sequence of operations on a single skyrmion in two spatial dimensions. Stack copies of the skyrmion to form a straight skyrmion tube. Keeping one end of the tube fixed, twist the top end by an angle of 2π about the tube axis which modifies the internal structure of the skyrmion along the tube. The ends of the twisted tube are identical. Therefore, they can be identified by bending the tube and gluing together the matching ends. A three-dimensional hopfion has been formed. If the tube had been twisted n times by 2π, the resulting hopfion would have had a Hopf index equal to nQ,

[1]Faculty of Physics and Center for Nanointegration Duisburg-Essen (CENIDE), University of Duisburg-Essen, 47057 Duisburg, Germany. [2]Institute of Physics, Johannes Gutenberg University Mainz, 55128 Mainz, Germany. [3]Department of Physics, University of Konstanz, 78457 Konstanz, Germany. ✉e-mail: karin.everschor-sitte@uni-due.de

where Q is the topological charge of the starting skyrmion. For hopfions in three spatial dimensions, the Hopf index is a homotopy invariant of the magnetization field map. Along any direction far way from a hopfion, at the so-called point at infinity, its magnetization converges to the same value; thus the three-dimensional space, via one-point compactification, adopts the topology of a three-sphere S^3. In the case of spatial hopfions, the magnetization field is a map from the compactified three-dimensional space S^3 to the space of possible magnetization directions S^2.

In the preceding abstract construction, the skyrmion tube was built by stacking skyrmion copies. It might as well have been generated from a skyrmion in two spatial dimensions whose texture is twisted as it evolved in time (see Fig. 1a). Moreover, such time evolution must be periodic so the temporal dimension, as implied by the gluing of the tube ends, has the topology of a circle (S^1). Equivalently, we require a skyrmion whose helicity, namely, the angle between the radial and the in-plane magnetization direction, periodically rotates in time. Therefore, to construct a spacetime magnetic hopfion we need a two-dimensional skyrmion with a time-periodic rotating helicity.

There is an alternative route to construct spacetime magnetic hopfions. Instead of one, it requires (at least) two spatially separated skyrmions. By braiding the skyrmions' center of mass positions we induce time-periodicity. Note that over the span of one period the skyrmions swap positions (see Fig. 1b). After identifying the swapped and initial skyrmion configurations, the resulting spacetime structure is topologically equivalent to a 2π-twisted skyrmion tube with its ends identified, and therefore to a spacetime magnetic hopfion.

Spacetime magnetic hopfions constructed from time-periodic, two-dimensional skyrmionic textures, as described above, have nontrivial spacetime topology. The topological invariant suitable for their characterization is the spacetime Hopf index

$$H = -\frac{1}{(8\pi)^2} \int dt \int d^2r \, \mathbf{A}_e \cdot \mathbf{B}_e, \qquad (1)$$

where $\mathbf{A}_e$ is the emergent gauge field satisfying $\mathbf{B}_e = \nabla \times \mathbf{A}_e$, $\mathbf{B}_e$ is the emergent magnetic field given by $B_{e,i} = \epsilon_{ijk}\mathbf{m} \cdot (\partial_j \mathbf{m} \times \partial_k \mathbf{m})$, with $\mathbf{m}$ the normalized magnetization, and $i, j, k \in \{x, y, t\}$. While the spatial integration is over the entire x-y plane, time is integrated over one period T.

For spacetime magnetic hopfions, unlike for hopfions in three-dimensional space, the base space is not S^3, but rather $S^2 \times S^1$; where the base space of the magnetic textures (skyrmions) is S^2, and the periodicity in time of the textures leads to the compactification of the temporal dimension to S^1. Because of this, the spacetime Hopf index H is no longer a homotopy

invariant of the system in general, but rather the skyrmion topological charge Q and the number of twists about the time axis n modulo $2Q$ are separately homotopy invariants[31-33]. Nevertheless, since $H = nQ$ and in our system Q is always equal to a nonvanishing constant (for instance, $Q = -1$ for a single skyrmion), H only depends on n and as long as $Q \neq 0$ the spacetime Hopf index can be regarded as a homotopy invariant.

In the following, we discuss how to concretely realize both routes to construct spacetime magnetic hopfions: by controlling the internal low-energy excitations (rotating helicity) of a single skyrmion, and by braiding the center of mass positions of multiple skyrmions.

Route 1: single skyrmion internal excitations

One route to construct spacetime magnetic hopfions relies on making the skyrmion helicity η time-periodic, i.e., $\eta(t) = \eta(t + T)$, where T is the period. However, the skyrmion-hosting magnetic material typically fixes the helicity at a value that is energetically favorable. Therefore, we first need to inject energy into the system, which will activate the internal excitations of the skyrmion and perhaps provide a way of controlling the helicity. These internal excitations might introduce unwanted multiply-periodic time dependence or, even worse, destabilize and eventually destroy the skyrmion itself. A more targeted strategy is to identify a class of skyrmion-hosting materials where the helicity is among the lowest-energy excitations. Even better, the lowest-energy one with vanishing excitation energy: a Goldstone mode.

The skyrmion helicity, in a minimal model (in particular in the absence of anisotropies), is known to be a Goldstone mode in frustrated magnets[34-37]. Therefore, in the absence of energy injection and dissipation, energy conservation enforces the skyrmion size to remain constant while allowing the helicity to rotate at a constant angular frequency. Another crucial property of frustrated magnets is that noncollinear magnetic textures, such as skyrmions, induce electric polarization $\mathbf{P}$[37-39]. An applied electric field $\mathbf{E}$ couples to the electric polarization as $\mathbf{E} \cdot \mathbf{P}$. This coupling provides a convenient, energy-efficient way to use a time-dependent applied electric field to control the magnetic skyrmion and hence, as we show below, its helicity.

Aiming to describe a broad class of frustrated magnets, we use the following rescaled micromagnetic energy functional

$$U = \int \left[-\frac{1}{2}(\nabla \mathbf{m})^2 + \frac{1}{2}(\nabla^2 \mathbf{m})^2 - \mathbf{B} \cdot \mathbf{m} - \mathbf{E} \cdot \mathbf{P} \right] d^3r, \qquad (2)$$

with adimensionalized external magnetic and electric fields $\mathbf{B}$ and $\mathbf{E}$ (see Methods). In the following, we set $\mathbf{B} = \hat{\mathbf{z}}$ and assume a thin film sample geometry. The interplay of the quadratic and quartic exchange terms

Fig. 1 | Spacetime magnetic hopfions—two construction routes based on skyrmion textures evolving periodically in time. a Helicity rotation: the helicity of a skyrmion rotates by 2π. **b** Skyrmion braiding: two skyrmions swap positions. Preimages (colored curves) trace four selected magnetization directions throughout one period T. Identifying the magnetic textures, and their corresponding preimages, at $t = 0$ and $t = T$, reveals their nontrivial spacetime topology. The preimages of the identified textures (insets) are linked, both corresponding to an $H = +1$ spacetime Hopf index.
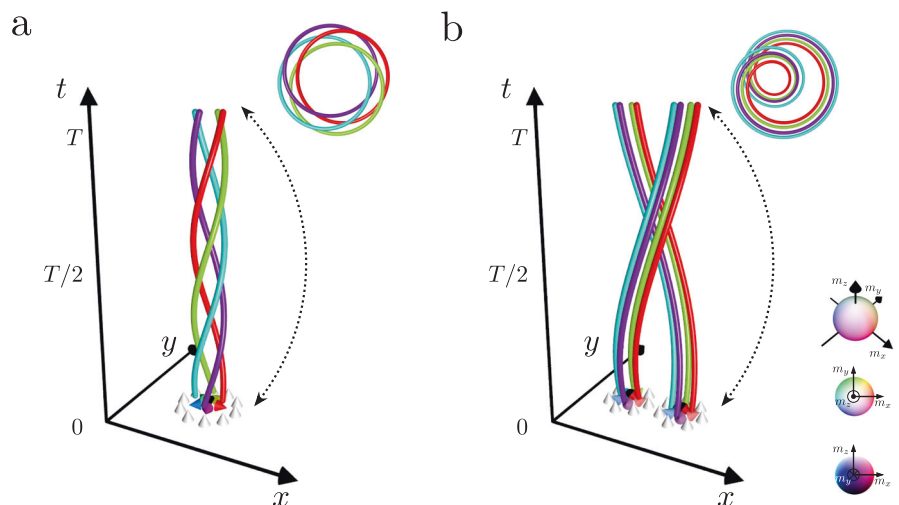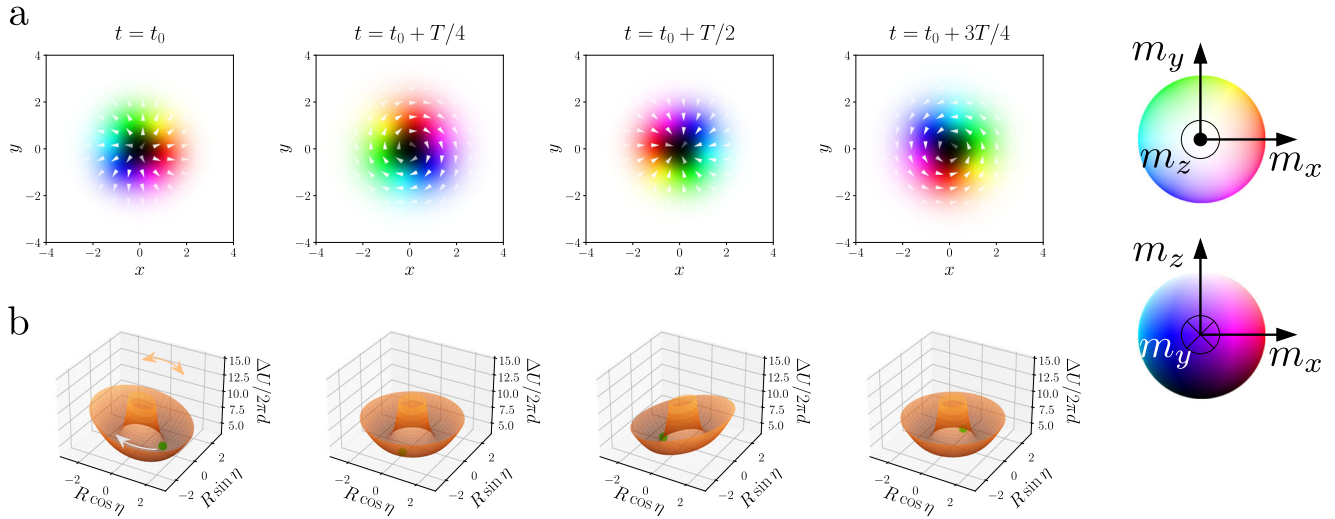
Fig. 2 | Time evolution of a skyrmion in a frustrated magnet driven by an AC electric field: activating helicity rotation. The skyrmion dynamics reaches a time-periodic steady state synchronizing to the driving electric field's period T. **a** Skyrmion texture snapshots, at $T/4$ intervals, from micromagnetic simulations confirm the T-periodic evolution. **b** Energy landscape snapshots as functions of the skyrmion collective coordinates, helicity η and radius R, shown in the $R\cos\eta - R\sin\eta$ plane with $\Delta U = U + \int d^3r\, \mathbf{B}\cdot\hat{\mathbf{z}}$ and sample thickness d. During one period, the energy landscape rocks back and forth about the $R\cos\eta = 0$ line as indicated by the orange arrow. The green dot represents the skyrmion collective coordinates time evolution. The direction of the helicity rotation (gray curved arrow) is uniquely defined by the driving electric field. Activating the T-periodic helicity rotation forms a spacetime magnetic hopfion. Parameters: $E_0 = 0.20$, $\omega = 2\pi/T = 1.18$, t_0 is deep in the steady state and $\eta(t_0) = 0 \pmod{2\pi}$; more details in Methods.

captures the details of the competing microscopic exchange interactions. The competing exchange terms give rise to a length scale, which, in the presence of a moderate out-of-plane magnetic field, stabilizes skyrmions[35]. Noncollinear magnetic textures, e.g. skyrmions, induce the electric polarization

$$\mathbf{P} = (\nabla \cdot \mathbf{m})\mathbf{m} - (\mathbf{m} \cdot \nabla)\mathbf{m}, \tag{3}$$

which couples to the applied electric field. The coupling has the form of an effective Dzyaloshinskii-Moriya interaction (DMI): $\mathbf{E} \cdot \mathbf{P} = D_{ik}^{j}(\mathbf{E})\, m_i \partial_j m_k$ with $D_{ik}^{j}(\mathbf{E}) = \epsilon_{ikm}\epsilon_{mlj}E_l$. Thus, the electric field allows the direct manipulation of the strength and sign of the effective DMI. For an electric field applied along the direction perpendicular to the thin film, the $\mathbf{E} \cdot \mathbf{P}$ coupling breaks rotational symmetry and provides control over the skyrmion helicity. Thus, this coupling allows an AC electric field to drive the frustrated magnet's magnetization dynamics and activate the helicity mode.

To model the electric-field-driven magnetization dynamics of a skyrmion we utilize two complementary approaches: micromagnetic simulations and collective coordinates. Our micromagnetic simulations employ the above micromagnetic energy functional, Eq. (2), together with the Landau-Lifshitz-Gilbert (LLG) equation (see Methods). In the collective coordinate modeling we focus on the two most relevant degrees of freedom: the skyrmion helicity η and, as a proxy for its canonically conjugate variable, the radius R. We derive their generalized Thiele equations, two coupled first-order nonlinear differential equations, which govern the joint skyrmion helicity and radius-driven dynamics, and we solve them numerically (see Methods). Both modeling approaches allow us to include energy injection from the driving AC electric field and energy dissipation from Gilbert damping, as expected in magnetic materials. Below, we show how to construct a spacetime magnetic hopfion by controlling the skyrmion dynamics driven by an alternating electric field.

An applied AC electric field $\mathbf{E}(t) = E_0\cos(\omega t)\hat{\mathbf{z}}$ drives the skyrmion dynamics. In this case, the electric field coupling induces a cosine helicity dependence, i.e. $\mathbf{E} \cdot \mathbf{P} \propto \cos\eta$. After the initial transient, the skyrmion dynamics reaches a time-periodic steady state with the same period $T = 2\pi/\omega$ of the driving AC electric field. Figure 2a shows selected snapshots of the skyrmion texture during such a steady state obtained from

micromagnetic simulations. The helicity executes a full rotation during one period of the applied AC electric field signaling the formation of a spacetime magnetic hopfion.

Further understanding of the driven helicity rotation follows from the micromagnetic energy, Eq. (2), depicted in Fig. 2b as a function of the collective coordinates, i.e. the skyrmion radius R and the helicity η. We find it convenient to plot the energy on the $R\cos\eta - R\sin\eta$ plane as it reflects the rotational invariance of the system in the absence of the electric field. The energy increases as the skyrmion shrinks below its equilibrium radius due to the quartic exchange interaction. In the presented collective coordinate model this yields an unphysical horn-shaped divergence at $R = 0$, which is an artifact of our skyrmion profile approximation for small radii. As the skyrmion expands beyond its equilibrium radius, the energy also increases due to the Zeeman term: $-\mathbf{B} \cdot \mathbf{m}$. Thus, there results an energy minimum trough. During one period the energy landscape rocks back and forth about the $R\cos\eta = 0$ line, such that the global energy minimum is at $\eta = \pi$ ($\eta = 0$) for $E_0 > 0$ ($E_0 < 0$). The amount of tilting is proportional to the electric field strength. The skyrmion's collective coordinates temporal evolution is represented by the green dot. The direction of the helicity rotation is uniquely defined by the applied drive, a feature that can be understood from the Thiele equations (see Methods for details)

$$\dot{R} = c_1\alpha + E_0\cos(\omega t)(c_2 + c_3\alpha) + \mathcal{O}(\alpha^2), \tag{4a}$$

$$\dot{\eta} = \dot{\eta}_0(R) + E_0\cos(\omega t)(c_4 + c_5\alpha) + \mathcal{O}(\alpha^2), \tag{4b}$$

where α is the damping parameter and the functions $c_1, \ldots, c_5$ depend on the collective coordinates. $\dot{\eta}_0(R)$ is the helicity rotation speed in the limit of $E_0 = 0$ and zero damping. In this limit, the magnetic energy U does not depend explicitly on the helicity (it is a Goldstone mode), and attains its minimum at the critical radius R^*. Therefore, the Thiele equations decouple and reduce to $\dot{R} = 0$ while $\dot{\eta} = \dot{\eta}_0(R)$ becomes only a function of R and swaps sign at a critical skyrmion radius R^*. For $R < R^*$, the helicity evolves clockwise (decreases, $\dot{\eta}_0 < 0$), while for $R > R^*$, it evolves counterclockwise (increases, $\dot{\eta}_0 > 0$), see Supplementary Note 1. In the presence of small damping and for $E_0 = 0$ the radius decreases to R^* and the speed of the helicity rotation decreases to zero. The electric field drives the helicity rotation actively and compensates for the damping.

Fig. 3 | Roadmap to construct spacetime magnetic hopfions by electric-field-driven helicity rotation. a Phase diagram of the long-term helicity dynamics, built from collective coordinate modeling with Gilbert damping $\alpha = 0.01$, of a skyrmion driven by an AC electric field with amplitude E_0 and frequency ω. The helicity rotates clockwise (counterclockwise) in the pink (green) regions leading to nonzero spacetime Hopf indices as indicated by the linked preimages of two selected points: with $H = -1$ (inset a(i)) and $H = +1$ (inset a(ii)). **b, c** Trajectories in the $R\cos\eta - R\sin\eta$ plane of the selected points from **a** with parameters $E_0 = 0.25$, $\omega = 0.72$ in **b**; and $E_0 = 0.20$, $\omega = 1.18$ in **c**. The trajectories are elliptical due to the skyrmion radius oscillations (breathing) shown in **d**. When the radius is larger (smaller) than R^*, the helicity increases (decreases) **e**, i.e., it rotates counterclockwise (clockwise).
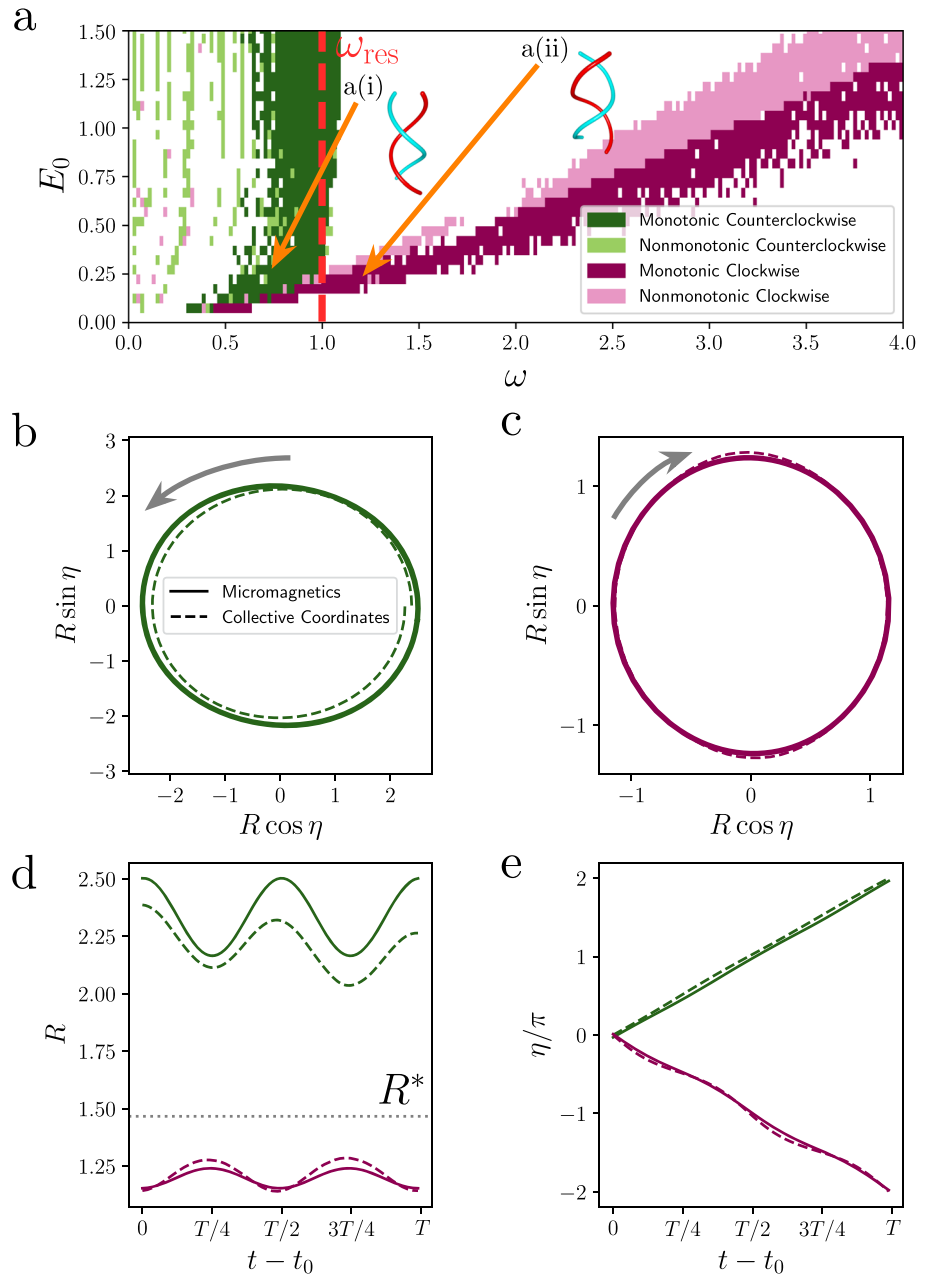
To investigate the conditions for helicity rotation required for a spacetime magnetic hopfion, we solved the Thiele equations for a range of electric field amplitudes E_0 and frequencies ω. From the steady-state solutions we built the phase diagram in Fig. 3a. In dark pink (dark green), we show solutions for which the skyrmion helicity rotates monotonically clockwise (counterclockwise), and in light pink (light green) the solutions for which the skyrmion helicity performs a non-monotonic but overall clockwise (counterclockwise) rotation. Below the pink region, the electric field amplitude is too low to induce a helicity rotation, while between the pink and dark green regions, the dynamics of the system are complex, and the helicity rotations do not synchronize with the electric field oscillation frequency. Helicity rotation solutions, the colored regions, cluster around two lobes.

In the leftmost lobe, dominated by counterclockwise helicity evolution (dark and light green regions), the Thiele equations predict the formation of spacetime magnetic hopfions with spacetime Hopf index $H = -1$. They form in the vicinity of the Kittel resonance frequency ω_{res}. Since our model does not include dipolar interactions, $\omega_{\text{res}} \propto B_z$; in dimensionless units,

having set $B_z = 1$, $\omega_{\text{res}} = 1$. Around the Kittel resonance frequency and for high E_0 energy injection supersedes dissipation. This imbalance is reflected in Thiele equations solutions with unphysically diverging skyrmion radii, signaling that the collective coordinate model is no longer adequate in this resonance region. While micromagnetic simulations of skyrmions in this region do not show diverging radii, they reveal spin wave emission and more complex skyrmion distortions. Even though the skyrmion helicity remains time-periodic, the resonance effects tend to disrupt the time periodicity of the skyrmion profile and thus the spacetime magnetic hopfion formation in this region. Nevertheless, in the rest of the leftmost lobe, the Thiele equations and micromagnetic simulations are in good agreement, as exemplified by the (solid and dashed) dark green trajectories in Fig. 3b, d, e. We conclude that in the leftmost lobe a low electric field amplitude E_0 and ω sufficiently far from ω_{res} ensure a moderate energy injection-dissipation imbalance and thus guarantee the formation of spacetime magnetic hopfions with $H = -1$.

The rightmost lobe comprises only clockwise helicity evolution (dark and light pink regions) corresponding to spacetime magnetic hopfions with

spacetime Hopf index $H = +1$. Here, resonance effects are absent, so the Thiele equations solutions and micromagnetic simulations are in good agreement, see e.g. the (solid and dashed) dark pink trajectories in Fig. 3c–e. Animations of the motion of the collective coordinates and the energy landscape for the clockwise and counterclockwise helicity rotations, for both selected points shown in Fig. 3, are shown in Supplementary Movies 1 and 2 respectively. The corresponding micromagnetic simulations are shown in Supplementary Movies 3 and 4. The energy injection rate is balanced by or slightly below the dissipation rate. Therefore, due to the balanced injection-dissipation ratio (see Supplementary Note 2), the absence of resonant effects, and a sizeable range of electric field amplitude and frequency, the rightmost lobe is an attractive region for the experimental realization of spacetime magnetic hopfions with $H = +1$.

A noteworthy feature of the right lobe is that the regions where the helicity evolution is monotonic (dark pink) and non-monotonic (pink) are separated by a straight line. This straight line coincides with Thiele equations solutions for which the maximum radius attained during a helicity rotation cycle equals R^* (see Supplementary Note 2). Therefore, for values of E_0 and ω in the pink region, the skyrmion radius crosses $R = R^*$ causing the helicity to reverse direction, thus becoming non-monotonic.

In the $\omega \lesssim 0.5$ region of the phase diagram, both clockwise (pink) and counterclockwise (green) rotating helicity steady states are present; for slow driving frequency allows the dynamical system to time-evolve close to the energy landscape bottom (see Fig. 2b), hence resulting in a rich structure of steady states.

The trajectories in the $R\cos\eta - R\sin\eta$ plane of two selected points on the phase diagram, depicted in Fig. 3b, c, have an elliptical shape. They reflect the coupled collective coordinate dynamics; helicity rotations are accompanied by skyrmion breathing, i.e. radial oscillations. When the radius is larger (smaller) than R^*, Fig. 3d, the helicity increases (decreases), Fig. 3e, which corresponds to counterclockwise (clockwise) rotations. For trajectories belonging to the phase diagram's leftmost (green) lobe, as in Fig. 3b, the radius attains its maxima at $\eta = 0, \pi$ and minima at $\eta = \pi/2, 3\pi/2$. The opposite holds for trajectories from the rightmost (pink) lobe, as in Fig. 3c, whose radius maxima are at $\eta = \pi/2, 3\pi/2$ and minima at $\eta = 0, \pi$. Since the helicity dependence of the micromagnetic energy comes solely from the coupling $\mathbf{E} \cdot \mathbf{P} \propto \cos\eta$, the rocking of the energy landscape (see Fig. 2b) gives trajectories with $R > R^*$ access to larger values of R along the $R\cos\eta$ than the $R\sin\eta$ axis. The situation reverses for trajectories with $R < R^*$. Therefore, the difference between these two elliptical trajectories boils down to the size of R relative to R^*.

When subjected to time-dependent perturbations of moderate intensity, as our stochastic LLG simulation study shows (see Supplementary Note 3), spacetime magnetic hopfions remain stable.

The above results confirm that spacetime magnetic hopfions are not rare and isolated, on the contrary, they can be constructed over a large range of frequencies and amplitudes of the driving electric field. Furthermore, the phase diagram in Fig. 3 provides a guide to tune between spacetime magnetic hopfions with opposite spacetime Hopf indices.

Route 2: multiple skyrmion braiding

An alternative construction route of spacetime magnetic hopfions follows from multiple skyrmion braiding. In this work, we treat magnetic skyrmions as classical, distinguishable objects. Braiding skyrmions requires exchanging their center of mass positions (see Fig. 1b). Controlling the position of skyrmions is crucial to many data storage and computing applications[40,41]. For instance, braiding skyrmions is at the core of a recent proposal for a topological quantum computing platform[42]. Therefore, the manipulation of skyrmion positions has rapidly developed and it is currently technologically advanced[14,43].

Control of skyrmion positions has been achieved in chiral, multilayer, and frustrated magnets. The breadth of mechanism to set individual skyrmions into motion include electric currents[44–49], tilted magnetic fields[50],

magnetic field gradients[51], temperature gradients[52], and circularly polarized laser illumination[53]. The above mechanisms can be modified to also induce rotational motion of skyrmion crystals[54]. Models to simulate the above mechanisms of driven skyrmion dynamics are already available.

Instead of simulating the dynamics of a particular model, here we focus on characterizing the spacetime topology arising from skyrmion braiding. We designed the magnetic texture of two skyrmions whose positions orbit each other (counterclockwise and clockwise) periodically over time. The period is defined by the time it takes the skyrmions to swap their positions. We then numerically computed their spacetime Hopf index. We find that for a counterclockwise swap (as in Fig. 1b) the Hopf index is $H = +1$, while for a clockwise swap $H = -1$.

It is conceptually straightforward to generalize the above construction to accommodate an arbitrary number of skyrmions. They could be assembled into skyrmion crystals, skyrmion bags[55,56], or engineered arrangements in nanopatterned substrates[42,57]. Braiding multiple skyrmions would result in spacetime magnetic hopfions with high spacetime Hopf indices.

Discussion

The two spacetime magnetic hopfion construction routes we have presented can be experimentally realized in various material platforms. Skyrmion braiding (construction route 2) requires controlling the skyrmion positions; this can be achieved by exploiting the experimentally reported skyrmion motion in the metallic chiral magnet FeGe[58,59], the insulating chiral magnet Cu_2OSeO_3[51,60,61], the van der Waals ferromagnet Fe_3GeTe_2[62], and in magnetic multilayers[63,64]. The rotation of the skyrmion helicity (construction route 1) is expected in frustrated magnets such as the skyrmion-hosting materials Gd_2PdSi_3[65], and $GdRu_2Si_2$[66]. Alternatively, we expect it to appear in skyrmion-hosting systems with tunable or weak DMI and for dynamically stabilized skyrmions where the helicity can be actively tuned[67,68].

Our spacetime magnetic hopfion constructions rely on magnetic textures whose spatial extension is two-dimensional; good approximations to this limit are the commonly fabricated thin films. Therefore, our modeling and simulations of frustrated magnets assume a thin film sample geometry, where (nonlocal) dipolar interactions, in the zero thickness limit, are well approximated by a (local) uniaxial magnetic anisotropy[69,70]. Magnetocrystalline anisotropies originate from spin-orbit coupling and hence are typically weaker than exchange interactions. Therefore, even though magnetocrystalline anisotropies tend to break spin-rotational symmetry that can hinder helicity rotations by introducing energy barriers, these are small and can be overcome by adjusting the external driving fields. Aiming at a simple and universal description, we have neglected anisotropies and dipolar interactions.

In frustrated magnets and multiferroics[71–74] the noncollinear magnetic texture of a single skyrmion induces electric polarization that in thin films gives rise to bulk and surfacebound electric charges. While the divergence of the polarization is proportional to the bound bulk charge density, the projection of the polarization onto the normal to the thin film surfaces determines the bound surface charge density. Although the net bound electric charge vanishes, the spatial distribution of the bound charge is localized near the skyrmion core. The oscillating radius of a breathing skyrmion makes its attached bound charge oscillate and hence radiate electromagnetic waves. Therefore, measuring this electromagnetic radiation could indirectly detect skyrmion breathing and, consequently, magnetic spacetime hopfions. Concretely, the bound charge surface densities at the thin film top and bottom surfaces are proportional to $\cos\eta$ and have opposite signs; thus a rotating helicity generates an oscillating electric dipole moment. For the systems studied in this work, the electric dipole radiation, the largest contribution from the multipole expansion, has a total power of ~10 fW. This estimated radiated power falls within the experimentally detectable range[75–77].

Direct detection of spacetime magnetic hopfions calls for measuring and tracking over time skyrmion magnetic textures; suitable for this purpose are Lorentz transmission electron microscopy (TEM)[78] and electron holography[79]. If the stability and time-periodic evolution of skyrmions in a particular system has already been established, it could be sufficient to just measure the helicity (construction route 1) or position (construction route 2). The skyrmion helicity can be extracted from Lorentz TEM measurements[80], and in the case of crystals or disordered ensembles of skyrmions, it can be measured using circularly polarized resonant elastic X-ray scattering[81]. Skyrmion position measurements have been reported using scanning transmission X-ray microscopy (STXM)[64,82,83], magneto-optical Kerr effect (MOKE) microscopy[63,84–86], and magnetic force microscopy (MFM)[87–90].

Conclusion

We have constructed spacetime magnetic hopfions. They are magnetic solitons whose spacetime structure, characterized by the spacetime Hopf index, carries nontrivial spacetime topology. We have shown two complementary construction routes that leverage the spatial topology of two-dimensional skyrmionic textures and a time-periodic drive: by skyrmion helicity rotation and by braiding skyrmions. Readily available experimental platforms to realize these construction routes of spacetime magnetic hopfions are frustrated magnets under an applied AC electric field, and chiral magnets or magnetic multilayers driven by an applied AC magnetic field. The principles we have used to construct spacetime magnetic hopfions can be applied beyond hopfions and magnetism. Other systems where topological solitons also emerge, might include liquid crystals, superfluids, superconductors, and electromagnetic fields. We envisage the time-periodic manipulation of solitons with low-dimensional spatial topology as a versatile method to develop high-dimensional spacetime topology. This method can become a tool for the active control of spacetime topology of general order parameters and fields.

Methods

The spacetime magnetic hopfions and, in particular, the electric-field-driven magnetization dynamics of a skyrmion considered in this work are modeled by the Landau-Lifshitz-Gilbert (LLG) equation[91,92]

$$\frac{\partial \mathbf{m}}{\partial t} = -\gamma \mathbf{m} \times \mathbf{B}_{\mathrm{eff}} + \alpha \mathbf{m} \times \frac{\partial \mathbf{m}}{\partial t}, \tag{5}$$

where γ is the electron gyromagnetic ratio, α is the Gilbert damping constant, and $\mathbf{B}_{\mathrm{eff}} = -M_s^{-1} \delta U / \delta \mathbf{m}$ is the effective magnetic field with the saturation magnetization M_s.

The dimensionful energy functional is given by

$$U = \int \left[-\frac{I_1}{2}(\nabla \mathbf{m})^2 + \frac{I_2}{2}(\nabla^2 \mathbf{m})^2 - M_s \mathbf{B} \cdot \mathbf{m} - \mathbf{E} \cdot \mathbf{P} \right] d^3 r, \tag{6}$$

where I_1 and I_2 are strengths of the quadratic and quartic exchange interactions, respectively, and $\mathbf{B}$ ($\mathbf{E}$) is the externally applied magnetic (electric) field. Noncollinear magnetic textures induce the electric polarization

$$\mathbf{P} = P_E a [(\nabla \cdot \mathbf{m})\mathbf{m} - (\mathbf{m} \cdot \nabla)\mathbf{m}], \tag{7}$$

where a is the lattice constant and P_E is the polarization density, which couples to the applied electric field. We define a natural length unit $\ell = \sqrt{I_2/I_1}$, a natural time unit $\tau = M_s I_2 / \gamma I_1^2$, a natural energy unit $\mathcal{U} = \sqrt{I_1 I_2}$, a natural applied magnetic field unit $\mathcal{B} = I_1^2 / M_s I_2$, a natural electric field unit of $\mathcal{E} = (\gamma / M_s^2)\sqrt{I_1^7 / I_2^3}$, and a natural polarization unit of $\mathcal{P} = (M_s^2/\gamma)\sqrt{I_2/I_1^3}$. This natural unit system is summarized in Supplementary Table 1. This rescaling leaves the theory with three parameters, the rescaled dimensionless externally applied fields and the Gilbert damping parameter, $\alpha = 0.01$ in this work.

Moreover, Eqs. (6) and (7) translate into Eqs. (2) and (3) in the main text. We have solved the skyrmion dynamics subjected to a periodic electric field using two complementary approaches: micromagnetic simulations and collective coordinates.

Micromagnetic simulations

For our micromagnetic simulations, we use the open-source micromagnetics simulation package MuMax3[93] with self-written extensions for the quartic exchange interaction and the electric field term. We neglect the effects of the demagnetizing field in our simulations for consistency with the collective coordinate modeling.

We consider a single-cell thin-film sample with $N = 128$ cells in x and y directions. Our system is discretized in cubic cells with edge length $\Delta = 0.3\sqrt{I_2/I_1}$. To suppress the reflection of spin waves from the thin film edges, we set $\alpha = 1$ over an area bordering the edges and extending up to 5 simulation cells into the sample.

We initialize our simulations with a skyrmion texture embedded in a ferromagnetic background and relax the system using the `Minimize()` function.

For the results shown in Figs. 2 and 3 we used $\alpha = 0.01$, $I_1 = 10^{-12}$ J m^{-1}, $I_2 = 10^{-29}$ J m and $M_s = 10^6$ A m^{-1}. For these parameter choices we obtain, for example, a magnetic field of 100 mT $= 1.0\, I_1^2 / M_s I_2$ and a typical length scale of 31.6 nm $\approx 10\sqrt{I_2/I_1}$ for a dimensionless magnetic field of 1.0 and a dimensionless length of 10. By micromagnetic simulations, we have also confirmed that we get the same results when we rescale the parameters according to Supplementary Table 1.

To calculate the radii of the skyrmions, we extract the contour for which $m_z = 0$ using the SCIKIT-IMAGE library[94], and calculate the mean of the displacements from the center of the contour. To compute the helicities, we extract the average helicity of the points on the $m_z = 0$ contour.

Collective coordinates

In the collective coordinate modeling[95,96] of the skyrmion, we employed rescaled units. We focus on the temporal dynamics of the two most relevant degrees of freedom: the helicity $\eta(t)$ and, as a proxy for its canonically conjugate variable, the radius $R(t)$[67].

Representing the magnetization by spherical angles, $\mathbf{m} = (\cos\phi \sin\theta, \sin\phi \sin\theta, \cos\theta)$, a rotationally invariant skyrmion texture centered at the origin of the xy plane is parametrized by its in-plane angle $\phi = \phi(\eta(t))$ and its profile function $\theta = \theta(R(t))$ which depend only on the skyrmion's helicity and radius, respectively. We assume that the film thickness d is sufficiently small such that magnetic textures can be considered uniform in the z-direction. While our model is effectively two-dimensional, we adopt the common practice of keeping a nonzero film thickness that can aid comparison with experimentally relevant parameters such as the exchange couplings, generally reported for three-dimensional systems and typically used in micromagnetic simulation codes such as MuMax3.

In this case, the effective equations of motions of the collective coordinate vector $\xi = (R, \eta)$ read $G_{ij}\dot{\xi}_j - \alpha\Gamma_{ij}\dot{\xi}_j + F_i = 0$ with the elements of gyrotropic G and dissipative Γ tensors, and generalized force F given by

$$G_{ij} = \int \mathbf{m} \cdot \left(\frac{\partial \mathbf{m}}{\partial \xi_i} \times \frac{\partial \mathbf{m}}{\partial \xi_j} \right) d^3 r, \tag{8a}$$

$$\Gamma_{ij} = \int \frac{\partial \mathbf{m}}{\partial \xi_i} \cdot \frac{\partial \mathbf{m}}{\partial \xi_j} d^3 r, \tag{8b}$$

$$F_i = -\frac{\partial U}{\partial \xi_i}. \tag{8c}$$

Only the generalized forces depend directly on the applied electric and magnetic fields. For symmetry reasons, the antisymmetric gyrotropic tensor has only one independent non-vanishing tensor element, i.e. $G_{R\eta} = -G_{\eta R}$ and $G_{RR} = G_{\eta\eta} = 0$, and the dissipative tensor is diagonal, i.e. $\Gamma_{\eta R} = \Gamma_{R\eta} = 0$. The effective equations of motion for the skyrmion's radial and helicity

temporal evolution become

$$\begin{bmatrix} \dot{R} \\ \dot{\eta} \end{bmatrix} = \frac{1}{G_{R\eta}^2 + \alpha^2 \Gamma_{RR}\Gamma_{\eta\eta}} \begin{bmatrix} \alpha\Gamma_{\eta\eta}F_R + G_{R\eta}F_\eta \\ -G_{R\eta}F_R + \alpha\Gamma_{RR}F_\eta \end{bmatrix}. \tag{9}$$

To solve Eq. (9) we use the following ansatz[97,98] for the skyrmion's in-plane angle ϕ and its profile function θ

$$\phi = m\psi + \eta(t), \tag{10a}$$

$$\theta = 2\arctan\left(\frac{\sinh(R(t)/w)}{\sinh(\rho/w)}\right), \tag{10b}$$

where $\rho = \sqrt{x^2 + y^2}$ and $\psi = \arctan(y/x)$ are the radial and angular polar coordinates, respectively. The skyrmion vorticity m is taken to be 1 in this work, and w characterizes the domain wall width of the skyrmion's profile. We find that for a domain wall width of $w = 1.4$, this ansatz approximates well the skyrmion obtained by micromagnetic simulations for both cases: in the relaxed state when the electric field is absent, as well as for excited skyrmions upon stimulation with the electric field. Using this ansatz, the remaining tensor elements are independent of the skyrmion's helicity and depend only on its radius R

$$G_{R\eta} = 2\pi d \int_0^\infty \rho\sin\theta\frac{\partial\theta}{\partial R}\,\mathrm{d}\rho, \tag{11a}$$

$$\Gamma_{RR} = 2\pi d \int_0^\infty \rho\left(\frac{\partial\theta}{\partial R}\right)^2 \mathrm{d}\rho, \tag{11b}$$

$$\Gamma_{\eta\eta} = 2\pi d \int_0^\infty \rho\sin^2\theta\,\mathrm{d}\rho. \tag{11c}$$

The generalized forces contain the information about the electric field breaking the rotational symmetry, which is why the electric field amplitude appears in combination with η:

$$F_R = E_0\cos(\omega t)\cos\eta\,2\pi d \int_0^\infty \left(\cos(2\theta)\frac{\partial\theta}{\partial R} + \rho\frac{\partial^2\theta}{\partial R\partial\rho}\right)\mathrm{d}\rho$$
$$- \frac{\partial U_{\mathrm{ex}}}{\partial R} - B_z 2\pi d \int_0^\infty \rho\sin\theta\frac{\partial\theta}{\partial R}\,\mathrm{d}\rho, \tag{12a}$$

$$F_\eta = -E_0\cos(\omega t)\sin\eta\,2\pi d \int_0^\infty \left(\cos\theta\sin\theta + \rho\frac{\partial\theta}{\partial\rho}\right)\mathrm{d}\rho, \tag{12b}$$

where $U_{\mathrm{ex}} = 2\pi d \int[-\frac{1}{2}(\nabla\mathbf{m})^2 + \frac{1}{2}(\nabla^2\mathbf{m})^2]\mathrm{d}\rho$ is the exchange interaction part of Eq. (2). Terms in F_R that are independent of E_0 depend only on R.

We numerically integrate the collective coordinates up to a dimensionless time of 1000 with an adaptive time step size. In obtaining the phase diagram in Fig. 3a, we took values in $0 \le E_0 \le 1.5$ and $0 \le \omega \le 4$ using meshes with step sizes of 0.05 and 0.02, respectively. To obtain the number of helicity rotations per electric field cycle, we integrated the changes of the helicity angles and averaged them over all periods for $500 \le t \le 1000$, neglecting the initial transient dynamics. Numerically, we classified a counterclockwise (clockwise) rotation as the average helicity rotation being greater than $0.9 * 2\pi$ (less than $-0.9 * 2\pi$). To perform the many numerical time integrations of $R(t)$ and $\eta(t)$ efficiently, we use the `multiprocessing` Python package and the Radau IIA integrator supplied by SciPy[99]. As initial conditions, we used the values of R and η that minimize the total energy Eq. (2) at $t = 0$.

To avoid the computationally intensive evaluation of the integrals over the radial coordinate at each time integration step in $G_{R\eta}$, Γ_{RR}, $\Gamma_{\eta\eta}$, F_R, and F_η, we employed fit functions of the corresponding integrals in the range $0 \le$ $R \le 10$. We verified that the error due to fitting the integrals was negligible. In particular, we found good agreement for cases where $R \lesssim 50$.

We have confirmed that an externally applied magnetic field with $B_z = 2$ leads to qualitatively the same results shown in Fig. 3a: with two lobes determining counterclockwise and clockwise helicity rotations and the resonance frequency being shifted to $\omega = 2$, as expected.

Data availability

Code availability

References
1. Kibble, T. W. B. Topology of cosmic domains and strings. *J. Phys. A Math. Gen.* **9**, 1387 (1976).
2. Rubakov, V.A., Gorbunov, D.S. *Topological Defects and Solitons in the Universe*, 2nd edn., 377–427 (World Scientific, 2017) https://doi.org/10.1142/9789813220041_0012.
3. Skyrme, T. H. R. A unified field theory of mesons and baryons. *Nucl. Phys.* **31**, 556–569 (1962).
4. Wallace, D. J. Solitons and instantons: An introduction to solitons and instantons in quantum field theory. *Phys. Bull.* **34**, 29 (1983).
5. Ryder, L.H. *Quantum Field Theory*, 2nd edn. (Cambridge University Press, Cambridge, 1996) https://doi.org/10.1017/CBO9780511813900.
6. Manton, N., Sutcliffe, P. *Topological Solitons* (Cambridge University Press, Cambridge, 2004) https://doi.org/10.1017/CBO9780511617034.
7. Dirac, P. A. M. Quantised singularities in the electromagnetic field. *Proc. R. Soc. Lond. A.* **133**, 60–72 (1931).
8. Sugic, D. et al. Particle-like topologies in light. *Nat. Commun.* **12**, 6785 (2021).
9. Shen, Y., Hou, Y., Papasimakis, N. & Zheludev, N. I. Supertoroidal light pulses as electromagnetic skyrmions propagating in free space. *Nat. Commun.* **12**, 5891 (2021).
10. Zdagkas, A. et al. Observation of toroidal pulses of light. *Nat. Photonics* **16**, 523–528 (2022).
11. Mermin, N. D. The topological theory of defects in ordered media. *Rev. Mod. Phys.* **51**, 591–648 (1979).
12. Heeger, A. J., Kivelson, S., Schrieffer, J. R. & Su, W.-P. Solitons in conducting polymers. *Rev. Mod. Phys.* **60**, 781–850 (1988).
13. Altland, A., Simons, B.D. *Condensed Matter Field Theory*, 2nd edn. (Cambridge University Press, Cambridge, 2010) https://doi.org/10.1017/CBO9780511789984.
14. Fert, A., Reyren, N. & Cros, V. Magnetic skyrmions: Advances in physics and potential applications. *Nat. Rev. Mater.* **2**, 1–15 (2017).
15. Everschor-Sitte, K., Masell, J., Reeve, R. M. & Kläui, M. Perspective: Magnetic skyrmions—Overview of recent progress in an active research field. *J. Appl. Phys.* **124**, 240901 (2018).
16. Back, C. et al. The 2020 skyrmionics roadmap. *J. Phys. D Appl. Phys.* **53**, 363001 (2020).
17. Masell, J., Everschor-Sitte, K. Current-induced dynamics of chiral magnetic structures: Creation, motion, and applications. In *Chirality, Magnetism and Magnetoelectricity: Separate Phenomena and Joint Effects in Metamaterial Structures*, (ed. Kamenetskii, E.) 147–181 (Springer International Publishing, Cham, 2021), https://doi.org/10.1007/978-3-030-62844-4_7.

18. Göbel, B., Mertig, I. & Tretiakov, O. A. Beyond skyrmions: Review and perspectives of alternative magnetic quasiparticles. *Phys. Rep.* **895**, 1–28 (2021).

19. Tokura, Y. & Kanazawa, N. Magnetic Skyrmion Materials. *Chem. Rev.* **121**, 2857–2897 (2021).

20. Zheng, F. et al. Magnetic skyrmion braids. *Nat. Commun.* **12**, 5316 (2021).

21. Hopf, H. Über die Abbildungen der dreidimensionalen Sphäre auf die Kugelfläche. *Math. Ann.* **104**, 637–665 (1931).

22. Faddeev, L. & Niemi, A. J. Stable knot-like structures in classical field theory. *Nature* **387**, 58–61 (1997).

23. Sutcliffe, P. Vortex rings in ferromagnets: Numerical simulations of the time-dependent three-dimensional Landau-Lifshitz equation. *Phys. Rev. B* **76**, 184439 (2007).

24. Sutcliffe, P. Skyrmion knots in frustrated magnets. *Phys. Rev. Lett.* **118**, 247203 (2017).

25. Rybakov, F. N. et al. Magnetic hopfions in solids. *APL Mater.* **10**, 111113 (2022).

26. Zhang, J. et al. Observation of a discrete time crystal. *Nature* **543**, 217–220 (2017).

27. Khemani, V., Moessner, R., Sondhi, S.L. A Brief History of Time Crystals. *ArXiv*, https://doi.org/10.48550/arXiv.1910.10745 (2019).

28. Träger, N. et al. Real-space observation of magnon interaction with driven space-time crystals. *Phys. Rev. Lett.* **126**, 057201 (2021).

29. del Ser, N., Heinen, L. & Rosch, A. Archimedean screw in driven chiral magnets. *SciPost Phys.* **11**, 009 (2021).

30. Bhowmick, D., Sun, H., Yang, B. & Sengupta, P. Discrete time crystal made of topological edge magnons. *Phys. Rev. B* **108**, 014434 (2023).

31. Auckly, D. & Kapitanski, L. Analysis of S^2-Valued Maps and Faddeev's Model. *Commun. Math. Phys.* **256**, 611–620 (2005).

32. Jäykkä, J. & Hietarinta, J. Unwinding in Hopfion vortex bunches. *Phys. Rev. D* **79**, 125027 (2009).

33. Kobayashi, M. & Nitta, M. Winding Hopfions on $R^2 \times S^1$. *Nucl. Phys. B* **876**, 605–618 (2013).

34. Leonov, A. O. & Mostovoy, M. Multiply periodic states and isolated skyrmions in an anisotropic frustrated magnet. *Nat. Commun.* **6**, 8275 (2015).

35. Lin, S.-Z. & Hayami, S. Ginzburg-landau theory for skyrmions in inversion-symmetric magnets with competing interactions. *Phys. Rev. B* **93**, 064430 (2016).

36. Zhang, X. et al. Skyrmion dynamics in a frustrated ferromagnetic film and current-induced helicity locking-unlocking transition. *Nat. Commun.* **8**, 1717 (2017).

37. Yao, X., Chen, J. & Dong, S. Controlling the helicity of magnetic skyrmions by electrical field in frustrated magnets. *N. J. Phys.* **22**, 083032 (2020).

38. Katsura, H., Nagaosa, N. & Balatsky, A. V. Spin current and magnetoelectric effect in noncollinear magnets. *Phys. Rev. Lett.* **95**, 057205 (2005).

39. Psaroudaki, C. & Panagopoulos, C. Skyrmion qubits: A new class of quantum logic elements based on nanoscale magnetization. *Phys. Rev. Lett.* **127**, 067201 (2021).

40. Fert, A., Cros, V. & Sampaio, J. Skyrmions on the track. *Nat. Nanotechnol.* **8**, 152–156 (2013).

41. Zhang, X., Ezawa, M. & Zhou, Y. Magnetic skyrmion logic gates: Conversion, duplication and merging of skyrmions. *Sci. Rep.* **5**, 9400 (2015).

42. Nothhelfer, J. et al. Steering majorana braiding via skyrmion-vortex pairs: A scalable platform. *Phys. Rev. B* **105**, 224509 (2022).

43. Li, S., Wang, X. & Rasing, T. Magnetic skyrmions: Basic properties and potential applications. *Interdiscip. Mater.* **2**, 260–289 (2023).

44. Jonietz, F. et al. Spin Transfer Torques in MnSi at Ultralow Current Densities. *Science* **330**, 1648–1651 (2010).

45. Komineas, S. & Papanicolaou, N. Skyrmion dynamics in chiral ferromagnets under spin-transfer torque. *Phys. Rev. B* **92**, 174405 (2015).

46. Woo, S. et al. Current-driven dynamics and inhibition of the skyrmion Hall effect of ferrimagnetic skyrmions in GdFeCo films. *Nat. Commun.* **9**, 959 (2018).

47. Zhang, X. et al. Static and dynamic properties of bimerons in a frustrated ferromagnetic monolayer. *Phys. Rev. B* **101**, 144435 (2020).

48. Xia, J. et al. Current-driven dynamics of frustrated skyrmions in a synthetic antiferromagnetic bilayer. *Phys. Rev. Appl.* **11**, 044046 (2019).

49. Hou, Z. et al. Current-Induced Helicity Reversal of a Single Skyrmionic Bubble Chain in a Nanostructured Frustrated Magnet. *Adv. Mater.* **32**, 1904815 (2020).

50. Moon, K.-W. et al. Magnetic bubblecade memory based on chiral domain walls. *Sci. Rep.* **5**, 9166 (2015).

51. Zhang, S. L. et al. Manipulation of skyrmion motion by magnetic field gradients. *Nat. Commun.* **9**, 2115 (2018).

52. Raimondo, E. et al. Temperature-gradient-driven magnetic skyrmion motion. *Phys. Rev. Appl.* **18**, 024062 (2022).

53. Tengdin, P. et al. Imaging the ultrafast coherent control of a skyrmion crystal. *Phys. Rev. X* **12**, 041030 (2022).

54. Everschor, K. et al. Rotating skyrmion lattices by spin torques and field or temperature gradients. *Phys. Rev. B* **86**, 054432 (2012).

55. Tang, J. et al. Magnetic skyrmion bundles and their current-driven dynamics. *Nat. Nanotechnol.* **16**, 1086–1091 (2021).

56. Kind, C. & Foster, D. Magnetic skyrmion binning. *Phys. Rev. B* **103**, 100413 (2021).

57. Nothhelfer, J., Hals, K.M.D., Everschor-Sitte, K., Rizzi, M. Method and device for providing anyons, use of the device. European Patent Application EP3751472A1/International Patent Application WO2020EP66120 (2019) .

58. Yu, X. Z. et al. Skyrmion flow near room temperature in an ultralow current density. *Nat. Commun.* **3**, 988 (2012).

59. Yu, X. Z. et al. Motion tracking of 80-nm-size skyrmions upon directional current injections. *Sci. Adv.* **6**, 9744 (2020).

60. Seki, S. et al. Formation and rotation of skyrmion crystal in the chiral-lattice insulator Cu_2OSeO_3. *Phys. Rev. B* **85**, 220406 (2012).

61. White, J. S. et al. Electric-Field-Induced Skyrmion Distortion and Giant Lattice Rotation in the Magnetoelectric Insulator Cu_2OSeO_3. *Phys. Rev. Lett.* **113**, 107203 (2014).

62. Ding, B. et al. Observation of Magnetic Skyrmion Bubbles in a van der Waals Ferromagnet Fe_3GeTe_2. *Nano Lett.* **20**, 868–873 (2020).

63. Jiang, W. et al. Mobile Néel skyrmions at room temperature: Status and future. *AIP Adv.* **6**, 055602 (2016).

64. Woo, S. et al. Observation of room-temperature magnetic skyrmions and their current-driven dynamics in ultrathin metallic ferromagnets. *Nat. Mater.* **15**, 501–506 (2016).

65. Kurumaji, T. et al. Skyrmion lattice with a giant topological Hall effect in a frustrated triangular-lattice magnet. *Science* **365**, 914–918 (2019).

66. Khanh, N. D. et al. Nanometric square skyrmion lattice in a centrosymmetric tetragonal magnet. *Nat. Nanotechnol.* **15**, 444–449 (2020).

67. McKeever, B. F. et al. Characterizing breathing dynamics of magnetic skyrmions and antiskyrmions within the hamiltonian formalism. *Phys. Rev. B* **99**, 054430 (2019).

68. Zhou, Y. et al. Dynamically stabilized magnetic skyrmions. *Nat. Commun.* **6**, 8193 (2015).

69. Winter, J. M. Bloch wall excitation. Application to nuclear resonance in a bloch wall. *Phys. Rev.* **124**, 452–459 (1961).

70. Rohart, S. & Thiaville, A. Skyrmion confinement in ultrathin film nanostructures in the presence of Dzyaloshinskii-Moriya interaction. *Phys. Rev. B* **88**, 184422 (2013).

71. Mostovoy, M. Ferroelectricity in spiral magnets. *Phys. Rev. Lett.* **96**, 067601 (2006).

72. Cheong, S.-W. & Mostovoy, M. Multiferroics: a magnetic twist for ferroelectricity. *Nat. Mater.* **6**, 13–20 (2007).

73. Seki, S., Yu, X. Z., Ishiwata, S. & Tokura, Y. Observation of skyrmions in a multiferroic material. *Science* **336**, 198–201 (2012).

74. Mostovoy, M. Electrically-Excited Motion of Topological Defects in Multiferroic Materials. *J. Phys. Soc. Jpn.* **92**, 081005 (2023).

75. Lo, H.-Y., Su, P.-C., Cheng, Y.-W., Wu, P.-I. & Chen, Y.-F. Femtowatt-light-level phase measurement of slow light pulses via beat-note interferometer. *Opt. Express* **18**, 18498–18505 (2010).

76. Kovalyuk, V. et al. On-chip coherent detection with quantum limited sensitivity. *Sci. Rep.* **7**, 4812 (2017).

77. Wang, X. et al. Oscilloscopic capture of 100 ghz modulated optical waveforms at femtowatt power levels. In *2019 Optical Fiber Communications Conference and Exhibition (OFC)*, pp. 1–3 (OFC, 2019) .

78. Yu, X. Z. et al. Real-space observation of a two-dimensional skyrmion crystal. *Nature* **465**, 901–904 (2010).

79. Park, H. S. et al. Observation of the magnetic flux and three-dimensional structure of skyrmion lattices by electron holography. *Nat. Nanotechnol.* **9**, 337–342 (2014).

80. Shibata, K. et al. Towards control of the size and helicity of skyrmions in helimagnetic alloys by spin–orbit coupling. *Nat. Nanotechnol.* **8**, 723–728 (2013).

81. Zhang, S. L., Laan, G., Wang, W. W., Haghighirad, A. A. & Hesjedal, T. Direct observation of twisted surface skyrmions in bulk crystals. *Phys. Rev. Lett.* **120**, 227202 (2018).

82. Woo, S. et al. Spin-orbit torque-driven skyrmion dynamics revealed by time-resolved X-ray microscopy. *Nat. Commun.* **8**, 15573 (2017).

83. Litzius, K. et al. Skyrmion Hall effect revealed by direct time-resolved X-ray microscopy. *Nat. Phys.* **13**, 170–175 (2017).

84. Jiang, W. et al. Direct observation of the skyrmion Hall effect. *Nat. Phys.* **13**, 162–169 (2017).

85. Vélez, S. et al. Current-driven dynamics and ratchet effect of skyrmion bubbles in a ferrimagnetic insulator. *Nat. Nanotechnol.* **17**, 834–841 (2022).

86. Quessab, Y. et al. Zero-field nucleation and fast motion of skyrmions induced by nanosecond current pulses in a ferrimagnetic thin film. *Nano Lett.* **22**, 6091–6097 (2022).

87. Casiraghi, A. et al. Individual skyrmion manipulation by local magnetic field gradients. *Commun. Phys.* **2**, 145 (2019).

88. Meng, K.-Y. et al. Observation of nanoscale skyrmions in $SrIrO_3$/$SrRuO_3$ bilayers. *Nano Lett.* **19**, 3169–3175 (2019).

89. Raju, M. et al. The evolution of skyrmions in Ir/Fe/Co/Pt multilayers and their topological Hall signature. *Nat. Commun.* **10**, 696 (2019).

90. Zhang, H. et al. Room-temperature skyrmion lattice in a layered magnet $(Fe_{0.5}Co_{0.5})_5GeTe_2$. *Sci. Adv.* **8**, 7103 (2022).

91. Landau, L., Lifshitz, E. 3 - On the theory of the dispersion of magnetic permeability in ferromagnetic bodies Reprinted from Physikalische Zeitschrift der Sowjetunion 8, Part 2, 153, 1935. In *Perspectives in Theoretical Physics*, (ed. Pitaevski, L.P.) 51–65 (Pergamon, Amsterdam, 1992) https://doi.org/10.1016/B978-0-08-036364-6.50008-9 (1992).

92. Gilbert, T. L. A phenomenological theory of damping in ferromagnetic materials. *IEEE Trans. Magn.* **40**, 3443–3449 (2004).

93. Vansteenkiste, A. et al. The design and verification of MuMax3. *AIP Adv.* **4**, 107133 (2014).

94. Walt, S. et al. scikit-image: image processing in python. *PeerJ* **2**, 453 (2014).

95. Tretiakov, O. A., Clarke, D., Chern, G.-W., Bazaliy, Y. B. & Tchernyshyov, O. Dynamics of domain walls in magnetic nanostrips. *Phys. Rev. Lett.* **100**, 127204 (2008).

96. Clarke, D. J., Tretiakov, O. A., Chern, G.-W., Bazaliy, Y. B. & Tchernyshyov, O. Dynamics of a vortex domain wall in a magnetic nanostrip: Application of the collective-coordinate approach. *Phys. Rev. B* **78**, 134412 (2008).

97. Braun, H.-B. Fluctuations and instabilities of ferromagnetic domain-wall pairs in an external magnetic field. *Phys. Rev. B* **50**, 16485–16500 (1994).

98. Wang, X. S., Yuan, H. Y. & Wang, X. R. A theory on skyrmion size. *Commun. Phys.* **1**, 31 (2018).

99. Virtanen, P. et al. SciPy 1.0: Fundamental Algorithms for Scientific Computing in Python. *Nat. Methods* **17**, 261–272 (2020).

100. Knapman, R., Tausendpfund, T., Díaz, S.A., Everschor-Sitte, K. Supplementary Codes for Spacetime Magnetic Hopfions: From Internal Excitations and Braiding of Skyrmions. *Zenodo*, https://doi.org/10.5281/zenodo.10869474.

Acknowledgements

Author contributions

K.E.-S. conceived the original idea with input from S.A.D and R.K. R.K. performed the collective coordinate modeling with support from S.A.D. and K.E.-S. The micromagnetic simulations were performed by R.K. and T.T. The data analysis and production of figures were performed by R.K. with support from the other authors. R.K. and S.A.D. wrote the manuscript with input from the other authors.

Funding

Competing interests

The authors declare no competing interests.

Additional information

Supplementary information The online version contains supplementary material available at https://doi.org/10.1038/s42005-024-01628-3.

Correspondence and requests for materials should be addressed to Karin Everschor-Sitte.

Peer review information This manuscript has been previously reviewed at another Nature Portfolio journal. The manuscript was considered suitable for publication without further review at *Communications Physics*.

Reprints and permissions information is available at http://www.nature.com/reprints

Publisher's note Springer Nature remains neutral with regard to jurisdictional claims in published maps and institutional affiliations.